
VINET: LIGHTWEIGHT, SCALABLE, AND HETEROGENEOUS COOPERATIVE PERCEPTION FOR 3D OBJECT DETECTION

Zhengwei Bai*, Guoyuan Wu, Matthew J. Barth

University of California, Riverside
Riverside, CA
zbai012@ucr.edu, gywu@cert.ucr.edu, barth@ece.ucr.edu

Yongkang Liu, Emrah Akin Sisbot, Kentaro Oguchi

Toyota North America InfoTech Labs,
Mountain View, CA
{yongkang.liu, akin.sisbot, kentaro.oguchi}@toyota.com

ABSTRACT

Utilizing the latest advances in Artificial Intelligence (AI), the computer vision community is now witnessing an unprecedented evolution in all kinds of perception tasks, particularly in object detection. Based on multiple spatially separated perception nodes, Cooperative Perception (CP) has emerged to significantly advance the perception of automated driving. However, current cooperative object detection methods mainly focus on ego-vehicle efficiency without considering the practical issues of system-wide costs. In this paper, we introduce VINet, a unified deep learning-based CP network for scalable, lightweight, and heterogeneous cooperative 3D object detection. VINet is the first CP method designed from the standpoint of large-scale system-level implementation and can be divided into three main phases: 1) Global Pre-Processing and Lightweight Feature Extraction which prepare the data into global style and extract features for cooperation in a lightweight manner; 2) Two-Stream Fusion which fuses the features from scalable and heterogeneous perception nodes; and 3) Central Feature Backbone and 3D Detection Head which further process the fused features and generate cooperative detection results. An open-source data experimental platform is designed and developed for CP dataset acquisition and model evaluation. The experimental analysis shows that VINet can reduce 84% system-level computational cost and 94% system-level communication cost while improving the 3D detection accuracy.

Keywords Cooperative Perception; 3D Object Detection; Deep Fusion; Artificial Intelligence; System-level Cost Analysis

1 Introduction

Throughout the world, transportation demand has increased in terms of the movement of people and goods on a daily basis. It is important to note, however, that a rapidly increasing number of vehicles has resulted in several major problems to the current transportation system, including safety [1], mobility [2], and environmental sustainability [3]. In order to improve system-wide performance, Cooperative Driving Automation (CDA) has emerged, leveraging recent advances in advanced sensing, wireless connectivity, and artificial intelligence. CDA enables connected and automated vehicles (CAVs) to communicate with one another, with the roadway infrastructure, and/or with pedestrians and cyclists equipped with mobile devices. In the past few years, CDA has gained increasing attention and is now considered a transformative solution to these challenges [4]. CDA applications are fundamentally dependent on object perception data from the surrounding environments, which is similar to the visual function of automated agents [5]. As the system

*Corresponding Author

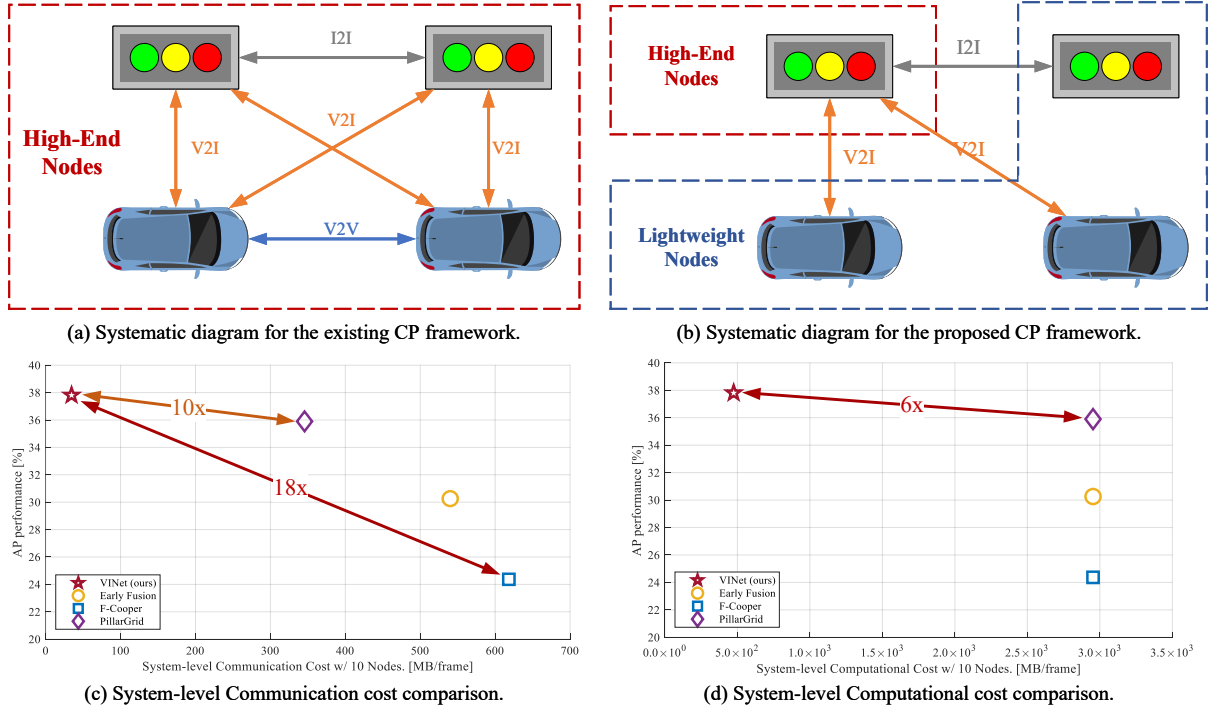


Figure 1: **The proposed framework for scalable, lightweight, and heterogeneous CP.** For a certain area, a central node is equipped with powerful computing resources while other nodes are only equipped with lightweight computing resources. Lightweight nodes will generate features for cooperation with limited computing power and the central node will generate the cooperative perception results and then broadcast to all road users (i.e., vehi. and infra.).

input, perception data can support a variety of CDA applications, such as Collision Warning [6], Eco-Approach and Departure (EAD) [7], and Cooperative Adaptive Cruise Control (CACC) [8].

In the past few decades, sensing technology has made it possible for transportation systems to retrieve high-fidelity traffic data from various types of sensors. The ability of situation awareness varies among different sensors both onboard vehicles or at the roadside. Cameras can provide detailed vision data for classifying various kinds of traffic objects, including vehicles, pedestrians, and cyclists [9]. On the other hand, high-fidelity 3D point cloud data can be retrieved by LiDAR sensors to grasp the precise 3D location of the traffic objects [10]. The robust performance of radar sensors in variable environmental conditions has made them an integral part of safety-critical automotive applications [11].

Perceiving the surrounding environment based on intelligent entities themselves has been one of the main methodologies to promote the development of Autonomous Driving Technology (ADT) [12, 10]. For automakers, automated vehicles are now equipped with more onboard sensors and powerful mobile computing that can process the massive amount of sensor data [13, 14]. Not only for onboard sensors, but recent researchers are now also conducting some studies that use infrastructure sensors that have the capability to perceive the traffic conditions at the object level [15, 16]. These different sensing entities can be regarded as spatially separated perception nodes (PNs) in a transportation system. Even when empowered with advanced perception methods, both Vehicle-based PNs (V-PNs) and Infrastructure-based PNs (I-PNs) have their specific and common limitations to perceiving the environment on their own. Specifically, V-PNs are inevitably limited by the occlusion of other road objects, while I-PNs are limited by the field of view (FOV) and blind zones. From a common point of view, neither V-PNs nor I-PNs themselves can perceive objects that are physically occluded or out of their sensing range. Thus to get past the bottleneck of single-PN perception, cooperation perception has emerged and is attracting increasing attention from researchers.

From an intuitive perspective, collaborating spatially separated PNs, i.e., Cooperative Perception (CP), naturally becomes a transformative solution to improving the perception breadth and accuracy. Therefore, numerous studies have been conducted to generate the perception information in a cooperative manner [17, 18, 19, 20, 21]. In terms of the stage of sensor fusion, CP can be divided into three main categories: 1) early fusion in which raw sensor data is shared

and combined [22], 2) late fusion in which perception results (i.e., bounding boxes) from each PNs are fused [17], and 3) deep fusion in which feature data from each PNs are shared and fused [19]. Different fusion schemes have their own merits and drawbacks. Early fusion only needs the calibration for aligning multi-source data into a unified coordinate system but requires a large communication bandwidth for transmitting data and is more sensitive to noise and delay [21] and is difficult to fuse multi-modal sensor data. Late fusion mainly focuses on how to merge the perception results generated from multiple perception pipelines, which is straightforward but suffers from limited accuracy [17]. Deep fusion is capable of generating high-performance perception results with low-communication requirements (compared to early fusion), but the development is still in its infancy and only a few studies have been conducted [18, 20].

Furthermore, due to the heterogeneity of V-PNs and I-PNs, only a couple of studies have focused on the vehicle-infrastructure CP [19, 21]. A real-world traffic scenario is always a dynamically changing system, which requires the CP methods to be able to cope with scalable PNs. Meanwhile, from the perspective of commercial deployment, it could be extremely costly to enable all PNs with powerful mobile computing units. However, to the best of our knowledge, the CP method that considers all the aspects mentioned above is still missing.

Hence, in this paper, we propose a cooperative perception network named *VINet (Vehicle-Infrastructure Network)*, a scalable and lightweight CP network that supports the cooperation of heterogeneous PNs. VINet mainly consists of five components: 1) Global Pre-Processing (GPP) which transforms the raw sensor data based on the global referencing coordinate; 2) Lightweight Feature Extraction (LFE) which generates deep features from raw sensor data with low-computational requirements; 3) Two-Stream Fusion (TSF) that fuses the features generated from scalable and heterogeneous PNs; 4) Central Feature Backbone (CFB) that extract hidden feature from the fused data; and 5) 3D Detection Head (3DH) that generates rotated 3D bounding boxes. The main contributions of this paper can be summarized as follows:

- We introduce the first unified CP framework to offer object detection with low system-level communication and computational cost;
- We propose VINet, the first deep learning-based scalable, lightweight, and heterogeneous CP method;
- We propose TSF, a novel deep-fusion model for heterogeneous feature data from scalable PNs; and
- We design and develop an open-source cooperative perception platform for supporting CP training and evaluation in scalable and heterogeneous environments.

The remainder of this paper is organized as follows: related work is reviewed in Section 2 to give a quick glance at the basic CP background. VINet is introduced in Section 3 with details of each consisting component. Section 4 illustrates experimental details about the training and evaluation process, followed by Section 6 that concludes the paper and highlights future work.

2 RELATED WORK

2.1 General 3D Object Detection From Point Clouds

Before 2015, one of the most popular mechanisms to handle point cloud data (PCD) from LiDAR sensors is the bottom-up pipeline based on traditional methods, such as “*Clustering [23]→Classification [24]→Tracking [25]*”. Due to their explainability and free from data labeling, traditional bottom-up methodologies are still popular in current infrastructure-based LiDAR perception tasks [26, 16, 27].

With the great success achieved by convolutional neural networks (CNNs) in image-based object perception, PCD quickly became the upcoming target for CNNs. Point-wise manipulation is considered straightforward for extracting features from PCD for object detection [28, 29]. Endowed with the natural fit, point-based methods provide dominant performance in detection accuracy, however, it scarifies computational efficiencies [30].

Since PCD consists of 3-dimensional sparse data, creatively cut the whole 3D point cloud into 3D voxels grids. A specific voting scheme, named *Vote3D*, was designed in 2015. In 2018, VoxelNet [31] was proposed, which introduced a learnable voxel encoder to generate hidden features of voxels. This voxelization mechanism has been widely used in various works, such as *SECOND [32]*, *PointPillar [33]*, *Voxel RCNN*

Projecting PCD into a 2D bird’s-eye view (BEV) feature map has quickly become a popular methodology. Inspired by YOLO, [34] proposed *ComplexYolo* which projected PCD into three manually defined feature channels, and then the BEV feature map was fed into a 2D backbone for generating detection results. Since the BEV scheme provides a straightforward way for solving 3D data in 2D manners, lots of BEV-based methods have emerged such as *PIXOR [35]*, *SCANet [36]*, *BEVFusion [37]*, etc.

2.2 Roadside LiDAR-based Object Detection

In recent years, roadside LiDAR sensors have received increasing attention from researchers about object perception in transportation [38]. Using roadside LiDAR, Zhao et al. proposed a detection and tracking approach for pedestrians and vehicles [16]. As one of the early studies utilizing roadside LiDAR for perception, a classical detection and tracking pipeline for PCD was designed. It mainly consists of 1) *Background Filtering*: To remove the laser points reflected from road surfaces or buildings by applying a statistics-based background filtering method [39]; 2) *Clustering*: To generate clusters for the laser points by implementing a Density-based spatial clustering of applications (DBSCAN) method 3) *Classification*: To generate different labels for different traffic objects, such as vehicles and pedestrians, based on neural networks [40]; and 4) *Tracking*: To identify the same object in continuous data frames by applying a discrete Kalman filter [25].

Based on the aforementioned work, Cui et al. designed an automatic vehicle tracking system by considering vehicle detection and lane identification [41]. In addition, a real-world operational system was developed, consisting of a roadside LiDAR, an edge computer, a *Dedicated Short-Range Communication (DSRC) Roadside Unit (RSU)*, a Wi-Fi router, and a *DSRC On-board Unit (OBU)*, and a GUI. Following a similar workflow, Zhang et al. proposed a vehicle tracking and speed estimation approach based on a roadside LiDAR [42]. Vehicle detection results were generated by the “*Background Filtering-Clustering-Classification*” process. Then, a centroid-based tracking flow was implemented to obtain initial vehicle transformations, and the unscented Kalman Filter [43] and joint probabilistic data association filter [44] were adopted in the tracking flow. Finally, vehicle tracking was refined through a BEV LiDAR-image matching process to improve the accuracy of estimated vehicle speeds. Following the bottom-up pipeline mentioned above, numerous roadside LiDAR-based methods have been proposed from various points of view [45, 46, 47, 48, 27].

On the other hand, using learning-based models to cope with LiDAR data is another primary stream. Bai et al. [49] proposed a deep-learning-based real-time vehicle detection and reconstruction system from roadside LiDAR data. Specifically, the CARLA simulator [50] was implemented for collecting the training dataset, and ComplexYOLO model [34] was applied and retrained for object detection. Finally, a co-simulation platform was designed and developed to provide vehicle detection and object-level reconstruction, which aimed to empower subsequent cooperative driving automation (CDA) applications with readily retrieved authentic detection data. In their following work for real-world implementation, Bai et al. [15] proposed a deep-learning-based 3D object detection, tracking, and reconstruction system for real-world implementation. The field operational system consisted of three main parts: 1) 3D object detection by adopting PointPillar [33] for inference from roadside PCD; 2) 3D multi-object tracking by improving DeepSORT [51] to support 3D tracking, and 3) 3D reconstruction by geodetic transformation and real-time onboard *Graphic User Interface (GUI)* display.

By combining traditional and deep learning algorithms Gong et al. [52] proposed a roadside LiDAR-based real-time detection approach. Several techniques were designed to guarantee real-time performance, including the application of Octree with region-of-interest (ROI) selection, and the development of an improved Euclidean clustering algorithm with an adaptive search radius. The roadside system was equipped with *NVIDIA Jetson AGX Xavier*, achieving the inference time of $110ms$ per frame.

2.3 Multi-Node Cooperative Object Detection

Although one single LiDAR can provide panoramic FOV around the ego-vehicle, physical occlusion may easily block the lines of sight and cause the ego-vehicle to lose some crucial perception information, which significantly affects its decision-making or control process. Additionally, a spatially separated LiDAR perception system can expand the perceptive range for intelligent vehicles or smart infrastructure.

One of the straightforward inspirations of the multi-LiDAR perception system is sharing the raw PCD via V2V communications [22]. However, limited wireless communication bandwidth may significantly limit real-time performance. Feature data generated from CNN requires much less bandwidth and is more robust to sensor noise, thus becoming a popular solution to multi-LiDAR fusion [18, 20]. Marvasti et al. [53] used two sharing-parameter CNNs to extract the feature map for PCD retrieved from two-vehicle nodes. Feature maps were then aligned based on the relative position and fused by element-wise summation. By applying an attention mechanism, Xu et al. [54] proposed a V2V-based cooperative object detection method. A similar CNN process [33] was designed for extracting feature maps for V2V sharing. Furthermore, self-attention was involved in data aggregation based on spatial location in the feature map.

Recently, researchers started focusing on cooperation between V-PN and I-PN based on the multi-LiDAR system. For handling the data heterogeneity from roadside and onboard PCD, Bai et al. [19] proposed a decoupled multi-stream CNN framework for generating feature maps accordingly. Relative position information was applied to PCD alignment and the shared feature maps were then fused based on grid-wise *maxout* operation. Additionally, Xu et al. [21] proposed a ViT-based CP method for heterogeneous PNs. Feature maps were extracted using sharing-parameter CNNs

Table 1: Summary of Different Fusion Schemes for Cooperative Perception [55].

Fusion Scheme	Methodology	Pros. and Cons.	Highlighted Features	Instance
Early Fusion	Deep Learning	Pros: Raw data is shared and gathered to form a holistic view.	Raw point cloud data is compressed to fit the limited bandwidth.	Chen et al. [22]
		Cons: Low tolerance to the noise and delay of the transmitted data; potentially constrained by the communication bandwidth.		
Deep Fusion	Deep Learning	Pros: High tolerance to the noise, delay, and difference between different nodes and sensor models.	Deep neural features are extracted and fused based on spatial correspondence.	Bai et al. [19]
		Cons: Require training data and hard to find a systematic way for model design.		
Late Fusion	Traditional	Pros: Easy to design and deploy in a real-world system.	A late-fusion is proposed based on joint re-scoring and non-maximum suppression.	Zhang et al. [56]
		Cons: Significantly limited by the wrong perception results or the difference between sources.		

and V2X communications. For dealing with heterogeneity, specific graph transformer structures were designed for data extraction.

3 Methodology

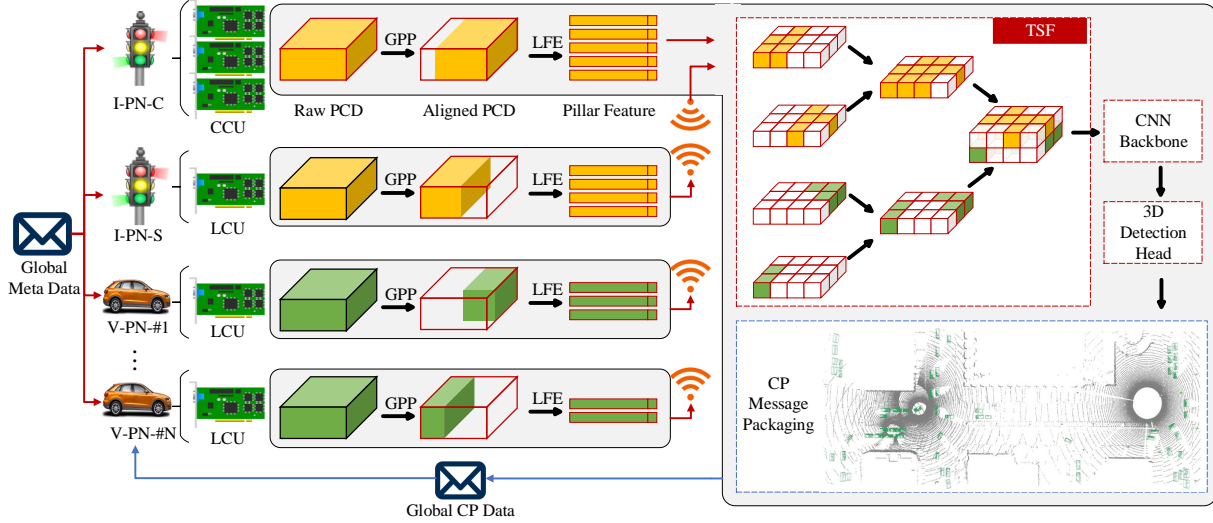


Figure 2: **Systematic diagram of the proposed cooperative perception system – VINet.** It consists of five components: Global Pre-Processing (GPP), Lightweight Feature Extraction (LFE), Two-Stream Fusion (TSF), Central Feature Backbone (CFB), and 3D Detection Head (3DH).

3.1 Overview of VINet

The main purpose of VINet is to reduce the system-wide computational cost by dividing the whole perception pipeline into two phases: 1) the lightweight feature extraction, and 2) the feature fusing and processing. Additionally, perception nodes (PNs) are categorized into two types: 1) *Central Nodes* which are equipped with powerful computing devices, named the Central Computing Unit (CCU), and 2) *Slave Nodes* which are equipped with Light-weight Computing Unit (LCU). In this paper, illustrated in Figure 2, one intersection PN (I-PN) is assigned as Central Node (I-PN-C) while other vehicle-PNs (V-PNs) and I-PN-S (I-PN-Slave) are assigned as Slave Nodes. Therefore, by assigning a lightweight feature extraction pipeline to Slave Nodes, only LCUs are needed for V-PNs and the I-PN-S. Thus, the whole cooperative perception (CP) system will only need one CCU and several LCUs to make CP available for every node with connectivity.

The network overview of VINet is shown in Figure 2. To reduce inter-node communication costs, Global Meta Data is designed and transmitted to all the PNs. From the system perspective, unlike previous CP methods which require

inter-node local-coordinate transformation [20, 21] with a communication cost of $\mathbf{O}(N^2)$, VINet only needs global transformation once for each node which has the communication cost of $\mathbf{O}(N)$ (N represents the number of PNs).

Based on Figure 2, the workflow of VINet can be summarized as follows:

- **Global Pre-Processing (GPP):** Based on LCU, raw PCD are transformed to the global coordinate and then geo-fenced within the predefined CP range.
- **Lightweight Feature Extraction (LFE):** based on LCU, globally aligned PCD are fed into a pillar feature extraction network to generate hidden features and transmit them to the Central Node.
- **Two-Stream Fusion (TSF):** based on CCU, pillar features from heterogeneous nodes are fused into a unified feature map.
- **Central Feature Backbone (CFB):** based on CCU, a multi-scale CNN backbone generate a feature map from fused feature data.
- **3D Detection Head (3DH):** based on CCU, detected bounding boxes are generated with class types for further broadcasting to all the connected nodes.

The following sections will introduce the aforementioned modules and details about the loss function applied in VINet.

3.2 Global Pre-Processing

3.2.1 Global Transformation

For global coordinate referencing, we design sensor calibration matrices that include the global 3D location and rotation information of the sensor, which is named as *Sensor Location and Pose* (SLaP) data. Raw PCD is originally recorded and organized in the 3D Cartesian coordinate with the center of the sensor of each node. Currently, one popular way of cooperative data transformation is to transform the PCD to the ego-vehicle’s coordinate [21], otherwise, there will exist spatial matching issues [18].

Since the PCD is collected based on a 3D Cartesian coordinate centered with the SLaP of the sensor, cooperative transformation is designed to unify the PCD from different sensors. The raw PCD can be described by:

$$P = \{[x, y, z, i]^T \mid [x, y, z]^T \in \mathbf{R}^3, i \in [0.0, 1.0]\} \quad (1)$$

The SLaP information is defined by the 3D location and rotation of the sensor:

$$\text{SLaP} = [X, Y, Z, P, \Theta, R] \quad (2)$$

where X, Y, Z, P, Θ , and R represent the 3D location along x -axis, y -axis, z -axis; and the pitch, yaw, and roll angles of the sensors in the global coordinate, respectively.

To avoid square-level inter-node communication which requires unreasonable system-wide communication costs, GPP aims to transform the PCD from PNs’ coordinates to a unified static global coordinate. Two main advantages of GPP compared with traditional inter-node transformation can be identified: 1) only linearly increasing communication cost is required for the whole CP system, and 2) a static global coordinate can have much less positioning error compared with the ego-vehicle coordinate.

3.2.2 Cooperative Geo-fencing

After the global transformation, a geo-fencing process is applied to PCD. In this paper, the detected region Ω for each of the LiDAR sensors is defined as a $280m \times 90m$ area centered at the location of the respective LiDAR. Specifically, $P_\Omega^{S \rightarrow G}$ is geo-fenced by:

$$P_\Omega^{S \rightarrow G} = \{[x, y, z, i]^T \mid x \in X, y \in Y, z \in Z\} \quad (3)$$

where $P_\Omega^{S \rightarrow G}$ represents the 3D point cloud data after geo-fencing; and X, Z and Y are defined by the CP range, which is further described in Section 4.2.

3.3 Lightweight Feature Extraction

Although deep features via the CNN backbone are intuitively suitable for CP tasks [18], it requires that every PNs have the capability of supporting the whole feature extraction pipeline. To distinguish our lightweight feature, the features generated after the whole CNN backbone are named *dense features*. In one of the popular deep fusion-based CP

methods, *F-Cooper* [18], dense features need to be calculated for all the involved PNs and then shared with each other. Since a CNN backbone is generally a deep neural network with a large amount of computing requirement [32, 57], deploying every PNs with powerful computing devices is a significant load for real-world implementation and commercialization. Additionally, dense features usually have a tremendous data size and thus they require powerful data compression techniques [20] to make the pipeline feasible in terms of real-time performance, which may inevitably cause perception performance drop and/or additional computing costs.

To reduce the computing requirement from the perspective of sharing feature extraction, a lightweight feature extraction (LFE) module is designed in this study. Inspired by [33], LFE aims to generate pillar features without the involvement of the CNN backbone, which can significantly reduce the computational loads on PNs. To cope with the heterogeneity of PCD from vehicles and infrastructures, two decoupled LFE blocks, i.e., vehicle LFE (V-LFE) and infrastructure LFE (I-LFE), are designed, which have the same network structure but different parameters.

For each LFE, the first part is to generate a D -dimensional feature vector V_p for all points in pillars:

$$V_p = \{[x, y, z, i, x_c, y_c, z_c, x_p, y_p]_i\}_{i=1}^N, p = 1, \dots, P \quad (4)$$

where $x_c, y_c, z_c, x_p, y_p, N$, and P represent the distance of each point to the arithmetic center of all points in the p -th pillar (the c subscript) and the geometrical center of the pillar (the p subscript), the number of points in the pillar and the number of pillars, respectively.

The second part is to extract the deep features of V_p by the following processes.

$$\mathcal{H}_{inf}^{(j)} = \max_{1 \leq i \leq N} (Dense_{inf}(\mathcal{F}_{inf}^{(j)})), j = 1, \dots, n \quad (5)$$

$$\mathcal{H}_{veh}^{(j)} = \max_{1 \leq i \leq N} (Dense_{veh}(\mathcal{F}_{veh}^{(j)})), j = 1, \dots, m \quad (6)$$

$$\mathcal{F}_{inf}^{(j)} = \{\{V_p^{(i)}\}_{i=1}^{P_j}\}_{j=1}^n \quad (7)$$

$$\mathcal{F}_{veh}^{(j)} = \{\{V_p^{(i)}\}_{i=1}^{P_j}\}_{j=1}^m \quad (8)$$

where $\mathcal{H}_{inf}^{(j)}$ and $\mathcal{H}_{veh}^{(j)}$ present the feature output from the LFE module which have the shape of (P_j, C) . Two decoupled MLP networks are designed as $Dense_{inf}(\cdot)$ and $Dense_{veh}(\cdot)$ to extract V_p from D -dimensional to C -dimensional. $\mathcal{F}_{inf}^{(j)}$ and $\mathcal{F}_{veh}^{(j)}$ present the feature data from j -th infrastructure/vehicle node.

3.4 Two-Stream Fusion

In this section, to combine the features from scalable and heterogeneous PNs, a specific feature fusion model, called *TSF*, is proposed. Since the roadside sensors and onboard sensors have different locations and poses, the point cloud distributions vary based on different sensor configurations. Although all those data can be transformed into a unified coordinate, the differences in data distribution still affect the fusion performance [19, 21]. Specifically, TSF consists of two main contributors, which are named *VI (Vehicle-Infrastructure) Stream* and *VI Fusion*, respectively. The whole fusion process can be formulated as:

$$\mathcal{S}_{inf} = \max_{1 \leq j \leq n} (Concat(\{\mathcal{M}(\mathcal{H}_{inf}^{(j)})\}_{j=1}^n)) \quad (9)$$

$$\mathcal{S}_{veh} = \max_{1 \leq j \leq m} (Concat(\{\mathcal{M}(\mathcal{H}_{veh}^{(j)})\}_{j=1}^m)) \quad (10)$$

$$\mathcal{H}_{cp} = \mathcal{C}(Concat(\mathcal{S}_{inf}, \mathcal{S}_{veh})) \quad (11)$$

where $\mathcal{M}(\cdot)$ is the designed mapping function to generate a 2D-pseudo-feature map from the LFE inputs; $Concat(\cdot)$ is the concatenation function to aggregate feature map H in each stream; \mathcal{S}_{inf} and \mathcal{S}_{veh} are the fused feature from each VI stream with a shape of $(1, C, H, W)$; \mathcal{H}_{cp} represents the output of TSF after a concatenation layer $Concat(\cdot)$ and a convolution layer $\mathcal{C}(\cdot)$.

Figure 3 is provided to further explain the TSF process. To consider the heterogeneity of features from different kinds of PNs, the core ideology of TSF is to create two separate feature streams to decouple the feature extraction and fusion within each class of PNs. For instance, as shown in , two dedicated LFEs are designed for extracting pillar features based on the data from vehicles and infrastructures, respectively. A regrouping process is applied to grouping those pillar features into two groups.

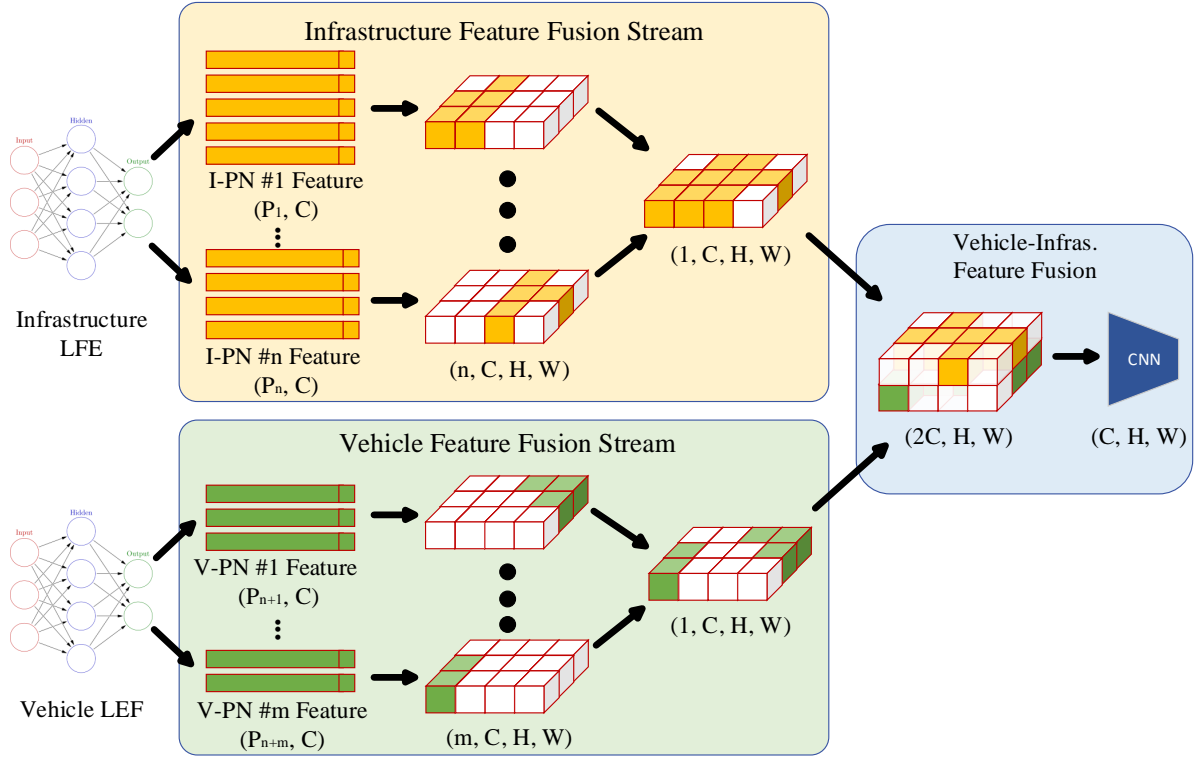


Figure 3: Illustration of the TSF process.

A feature mapping process is implemented for each group of features to generate a 2D spatial feature map for each PN in this group, e.g., feature tensor with the shape of (n, C, H, W) for the infrastructure stream. Based on the previous GPP process, the feature maps from different PNs are spatially aligned with the global coordinate already. Then, a fusion process is designed to fuse features from different nodes while keeping their heterogeneity. At the end of the VI stream, features from each stream will be extracted into a $(1, C, H, W)$ tensor. The fused features for each stream are then fused using VI fusion to form a $(2C, H, W)$ feature tensor. Finally, a CNN fuses the $(2C, H, W)$ tensor into the shape of (C, H, W) to keep a consistent spatial shape of output.

3.5 Central Feature Backbone

Based on the centralized design, VINet only needs one CNN backbone, named Central Feature Backbone (CFB), for the whole CP system for all PNs. To make a fair comparison with others, a classic Region Proposal Network (RPN) [31] is implemented as the CFB in VINet. It is noted that from a theoretical standpoint, since the central PN is equipped with CCU, CFB can be a more powerful backbone to further squeeze the performance of fused features.

The CFB consists of three phases: 1) *Downsample CNN*, which consists of several 2D CNN blocks (*Conv2D*) to extract the features in a spatial downsampling manner, 2) *Upsample CNN*, which consists of several deconvolutional blocks (*DeConv2D*) to extract the features in a spatially upsampling manner, and 3) *Multi-scale fusion*, which concatenates the output of each *DeConv2D* to gain multi-scale feature for each spatial location.

3.6 3D Detection Head

To generate 3D rotated bounding boxes, an anchor-based 3D dense head [33] is applied for all the models. Intersection over Union (IoU) is implemented to match the prior bounding boxes with the ground truth. Additionally, both pedestrians and vehicles are considered.

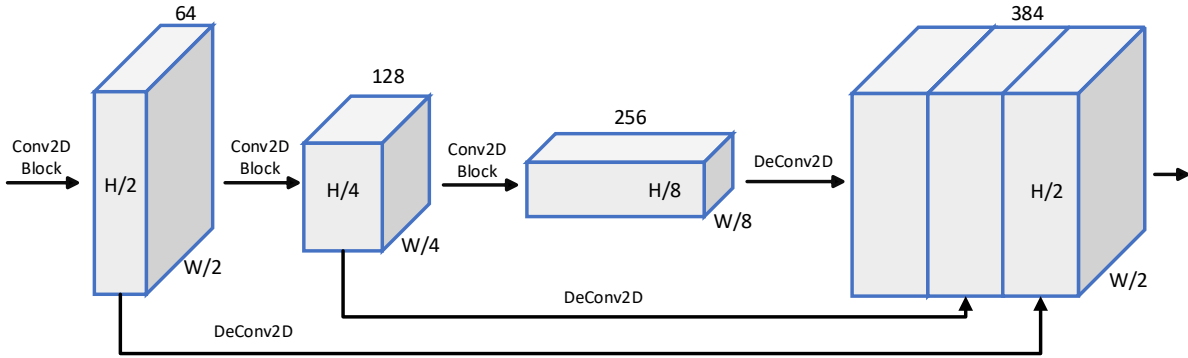


Figure 4: Illustration of the CFB structure which consists of Convolutional and Deconvolutional blocks.

4 Experiments

4.1 Dataset Acquisition

Considering the requirement of cooperative perception (CP) research, a platform is needed for customized dataset acquisition. Thus, a CP platform has been designed and developed to support CP model training and validation, such as sensor data collecting and ground truth labeling. We build a CP platform on top of the CARLA simulator [50] for data collection. In addition, to ease the re-usability and accessibility, we organize the new dataset to be compatible with existing open-source training platforms (e.g., OpenMMLab [58]), by following the KITTI’s format [59]. Nonetheless, the KITTI’s settings and the CARLA have different coordinate systems, so a conversion is used to generate the ground truth labels in the KITTI coordinates.

All the sensors are synchronized based on CARLA and the simulation is running at 10Hz while the data frame is collected at 2Hz to increase the variety of the whole dataset (i.e., same strategy as NuScenes [60]). Literally, from our CP platform, unlimited frames of data can be collected with nearly zero cost. In this paper, for speeding up the experimental process, 8,695 frames of 3D point clouds are collected, including 4347 frames for training, 1449 frames for evaluation, and 2899 frames for testing.

Furthermore, the LiDAR settings for onboard and roadside are different. Detailed specifications of those Lidar sensors are described in Table 2. The main differences lie in the heights and FOVs.

Table 2: Parameter Configuration and Description for the 3D-LiDAR Sensors (onboard/roadside) Deployed in the CARTI Platform

Parameters	Default	Description
Channels	64	Number of lasers.
Height	1.74/4.74m	Height above the ground.
Range	100.0m	Maximum distance to measure/ray-cast in meters.
Frequency	10.0Hz	LiDAR rotation frequency.
Upper FOV	+22.5 / +0	Angle in degrees of the highest laser beam.
Lower FOV	-22.5 / -22.5	Angle in degrees of the lowest laser beam.
Reflection rate	0.004	Coefficient that measures the LiDAR intensity loss.
Noise stdev	0.01	The standard deviation of the noise model of points.
Dropoff rate	45%	General proportion of points that are randomly dropped.
Dropoff intensity	0.8	The threshold of intensity value for exempting dropoff.
Dropoff zero intensity	40%	The probability value of dropoff for zero-intensity points.

4.2 Experimental Setup

For the purpose of evaluating and investigating the CP performance of leveraging multiple PNs, the CP scenario (shown in Figure 1) is set as a two-adjacent intersection area with $280m \times 80m$, which is much larger than a single-node perception area. Specifically, in Figure 1, the western infrastructure is defined as the I-PN-C whose coordinate is also set as the reference of the global coordinate. Thus, for GPP, the specific perception field is in the range of $x \in [-53.76m, 181.76m]$ and $y \in [-48.6m, 41m]$. For LFE, both PCD from the roadside LiDARs and onboard LiDARs are transformed into pillars with the voxel size of $[0.23m, 0.23m, 4.0m]$ in this paper, the maximum number of pillars for each node is set as $[25, 000, 15, 000]$ for training and testing. For CFB, each Conv2D block consists of one Conv2D layer with the kernel of $(3, 2, 1)$, followed by several Conv2D layers with kernels of $(3, 1, 1)$. Specifically, the numbers of Conv2D layers in each block are 4, 6, and 6, respectively. For 3DH, the number of object classes is set to be 2, i.e., car and pedestrian.

4.2.1 Training Details

The training and testing platform is equipped with Intel[®] Core[™] i7-10700K CPU@3.80GHz \times 16 and NVIDIA GPU@GeForce RTX 3090. The training pipeline is designed with 160 epochs with *Batchsize* of 2. During training, a data sample strategy is applied by filtering the ground target by minimum points (MP) reflected by LiDAR. Specifically, MP is set as 5 and 10 for car and pedestrian objects, respectively.

4.2.2 Evaluation Matrix

- **True Positive (TP)**: the number of cases predicted as positive by the classifier when they are indeed positive, i.e., a vehicle object is detected as a vehicle.
- **False Positive (FP)** = the number of cases predicted as positive by the classifier when they are indeed negative, i.e., a non-vehicle object is detected as a vehicle.
- **True Negative (TN)** = the number of cases predicted as negative by the classifier when they are indeed negative, i.e., a non-vehicle object is detected as a non-vehicle object.
- **False Negative (FN)** = the number of cases predicted as negative by the classifier when they are indeed positive, i.e., a vehicle is detected as a non-vehicle object.

Precision is the ability of the detector to identify only relevant objects, i.e., vehicles and pedestrians in this paper. It is the proportion of correct positive predictions and is given by

$$Precision = \frac{TP}{TP + FP} = \frac{TP}{\# \text{ of all detections}} \quad (12)$$

Recall is a metric that measures the ability of the detector to find all the relevant cases (that is, all the ground truths). It is the proportion of TP detected among all ground truth (i.e., real vehicles) and is defined as

$$Recall = \frac{TP}{TP + FN} = \frac{TP}{\# \text{ of all ground truth}} \quad (13)$$

The detection performance is measured with Average Precision (AP) and Average Recall (AR) at Intersection-over-Union (IoU) thresholds of 0.25 for pedestrians and 0.7 for cars, respectively. Furthermore, based on the MP reflected by the ground target, each evaluation class is further divided into three categories: $MP \geq 10$, $MP \geq 5$, and $MP \geq 1$, respectively, to investigate the performance of CP methods on different difficulty levels.

4.2.3 Compared Baselines

Three baselines are selected from different perspectives: 1) **Raw PCD fusion** – *EarlyFusion* based on *PointPillar* [33] is considered as it is one of the most straightforward CP methods; 2) **Dense CNN-feature fusion** – *F-Cooper* [18] is considered since it provides a classic fusion scheme by fusing the feature map generated by the CNN backbone; and 3) **Pillar feature fusion** – our last baseline is *PillarGrid* [19], the first CP method that uses pillar features for fusion. To make a fair comparison, all methods are trained based on the same CNN backbone and 3D detection head with the same training epochs. All the other data sampling and augmentation techniques are set the same for all methods.

Table 3: AP Results on the CARTI Dataset Using the BEV Detection Benchmark

Model	Feature Type	Overall AP	Pedestrains AP@0.25			Car AP@0.7		
			MP \geq 10	MP \geq 5	MP \geq 1	MP \geq 10	MP \geq 5	MP \geq 1
Early Fusion	Raw PCD	35.20	7.23	9.39	10.47	61.79	61.57	60.74
F-Cooper	Dense CNN	27.46	4.38	11.63	12.34	46.35	46.34	43.71
PillarGrid	Pillar Feature	39.48	7.49	10.81	12.87	70.42	69.13	66.17
VINet	Pillar Feature	41.49	8.21	15.48	18.07	70.83	70.11	66.22

Table 4: AP Results on the CARTI Dataset Using the 3D Detection Benchmark

Model	Feature Type	Overall AP	Pedestrains AP@0.25			Car AP@0.7		
			MP \geq 10	MP \geq 5	MP \geq 1	MP \geq 10	MP \geq 5	MP \geq 1
Early Fusion	Raw PCD	30.26	6.94	8.56	9.34	52.39	52.27	52.08
F-Cooper	Dense CNN	24.37	4.28	11.42	12.15	40.49	39.91	37.96
PillarGrid	Pillar Feature	35.90	6.58	10.09	12.16	62.28	62.21	62.06
VINet	Pillar Feature	37.81	7.58	14.83	17.16	62.51	62.44	62.31

4.3 Quantitative Evaluation

4.3.1 Object Detection

The numerical testing results are illustrated in Table 3 and 4. Two evaluation benchmarks are involved: the BEV detection benchmark and the 3D detection benchmark. Table 3 demonstrates the performance on the BEV benchmark. VINet dominates all the compared methods. Specifically, VINet can improve the overall mAP by +6.29%, +14.03%, and +2.01% compared with Raw PCD fusion [33], Dense CNN-feature fusion [18], and pillar-feature fusion [19]. Furthermore, for general pedestrian detection (i.e., $MP \geq 1$), VINet significantly improves the mAP by over +5% for all other methods.

For 3D detection results shown in Table 4, VINet can offer the mAP improvements by +7.55%, +13.44%, +1.91% compared with EarlyFusion, F-Cooper, and PillarGrid respectively. Additionally, for car detection, the pillar feature-based methods can bring tremendous performance improvement, such as 10 + % mAP than early fusion and 20 + % mAP than Dense CNN-based fusion.

4.3.2 Real-time Inference

Table 9 also demonstrates the computing speed of the real-time inference pipeline. Both VINet and EarlyFusion can process over 10 frames per second, while F-Cooper can only get 8 frames. Considering that the real-time LiDAR rotating speed is 10Hz, it demonstrates that VINet also has the capability for real-time inference.

4.4 Qualitative Results

Figure 5 shows the visualization CP results of all the methods in the same data frame under different numbers of PNs.

4.4.1 Object Detection

From the perspective of vehicle detection, both VINet and PillarGrid surpass the EarlyFusion and F-Cooper. It is also demonstrated that pillar feature-based cooperation can achieve better performance compared with raw point-based fusion and dense feature-based fusion. In terms of pedestrian detection, VINet surpasses all the baselines, which demonstrates that TSF has a better capability of extracting and fusing features for small objects.

4.4.2 Various Number of PNs

Regarding the number of PNs, when it grows from 3 to 7, feature-based methods, e.g., VINet, PillarGrid, and F-Cooper, can maintain their performance, while EarlyFusion has an evident performance drop. One hypothetical reason is when a single object is perceived by multiple sensors, feature data is more consistent than raw PCD. For instance, if

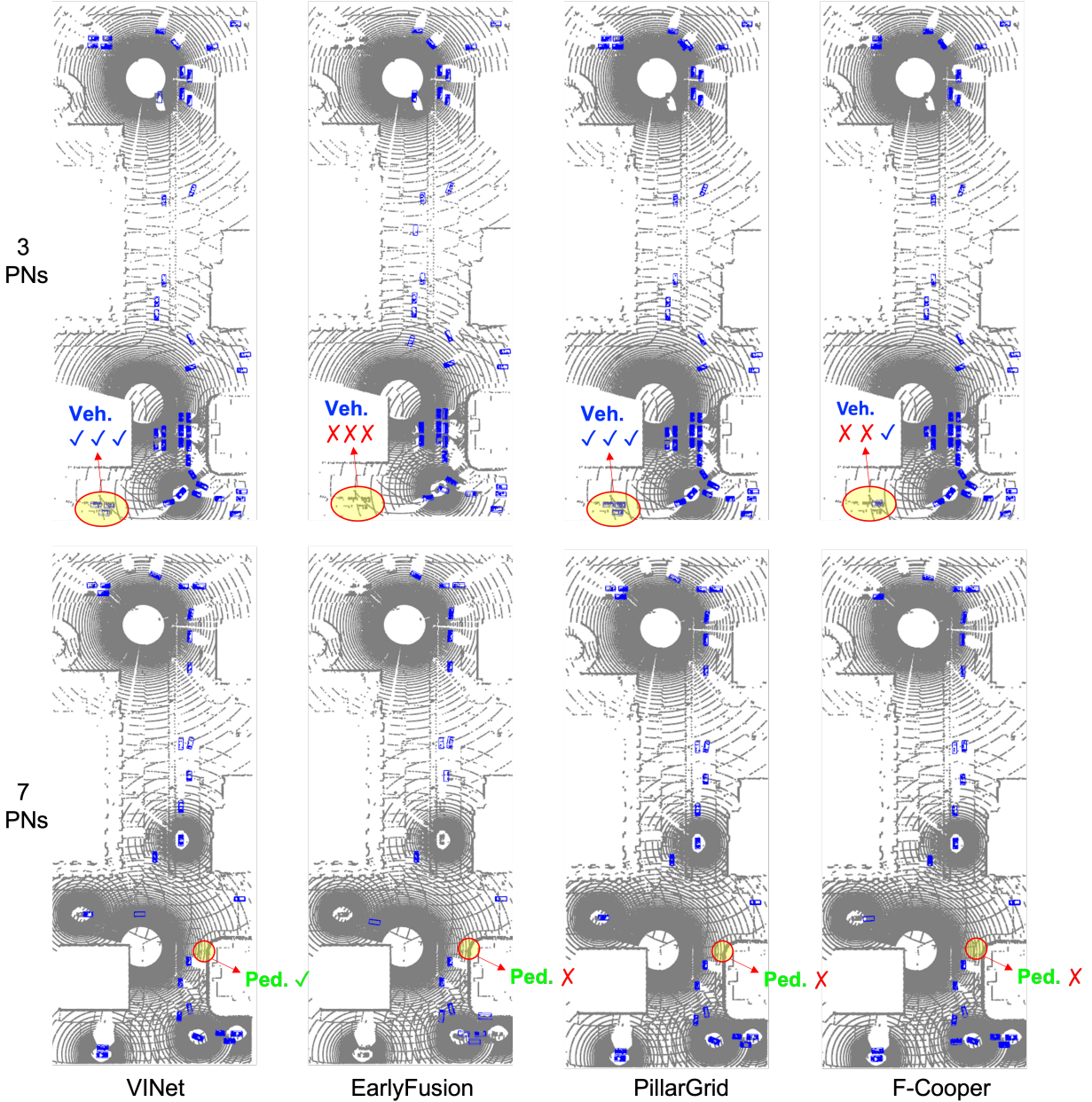


Figure 5: Visualization results for different methods under different numbers of PNs (top row: 3 PNs, bottom row: 7 PNs).

a car is perceived by two LiDARs (one from the front while another from the back), the raw PCD information reflected by this car from those two LiDARs has a bigger difference than the deep feature extracted from the neural networks. In another word, since the neural nets, especially CNN, act like a filtering process, we can infer that feature data from single objects tend to have a smaller divergence than raw PCD. Thus, feature data is also more suitable for large-scale CP systems than raw data.

4.5 Ablation Study

In this section, we provide ablation studies and analyze the key design of VINet. From Table 5, both the VI stream and VI fusion contribute to the detection performance for pedestrians and vehicles.

Table 5: Component Ablation Study for: i) VI Stream and ii) VI Fusion under 3D Benchmark with $MP \geq 1$.

VI Stream	VI Fusion	Pedestrian	Vehicle
×	×	9.73	22.15
✓	×	14.33	61.41
×	✓	12.16	62.07
✓	✓	17.16	62.31

4.5.1 Two Stream Structure

VI stream significantly impacts the small object detection, i.e., AP +5% for pedestrians, which implies that the two stream structure can better handle the heterogeneity of sensors.

4.5.2 Feature Fusion Scheme

Without the TSF structure, the performance will drop drastically for vehicles, i.e., AP −40.16%, and moderately for pedestrians, i.e. AP −4.60%. This indicates that the TSF plays a vital role for feature fusion. A hypothesis is that vehicles are much larger than pedestrians, and therefore their detection can benefit more from the fused features than only from the single feature.

5 System-Level Cost Analysis

In this section, we will comprehensively analyze the computational cost and communication cost from the stand-point of system-level application. We categorize cooperative perception into two types: egocentric CP and holistic CP, which are distinguished by the difference in beneficial nodes. For instance, in most of the recent cooperative perception works [18, 54, 20], a basic hypothesis under these CP methods is that only one perception node is performing cooperative perception while other nodes only act as the subsidiary to provide feature information to benefit the ego-vehicle. Thus, we define this kind of CP as egocentric CP.

Conversely, if all the vehicles are permutation-invariant or, in another word, every vehicle will share information with others to enhance everyone’s perception in the network, we define this type of CP as holistic CP. From the perspective of realistic implementation, it may be more beneficial to implement the holistic CP system in the real world. However, the computing complexity of a holistic CP system would be extremely high if no specific optimizations are conducted to the perception structure.

Thus, we evaluate VINet by comparing it with multiple different baselines as well as under different cooperative perception conditions. Both theoretical analysis and experimental analysis are conducted and shown below.

5.1 Theoretical Cost Analysis

5.1.1 Computational Complexity

To analyze the computational complexity of a model, the total number of computations the model has to perform is an important factor. In this paper, we adopt the Floating Point Operations (FLOPs), which apply to any type of computing operations that involve a floating point value. Generally, the more FLOPs the model has to perform, the more complex the model is. In addition to FLOPs, we also involve Multiply-Accumulate Computations (MACs) to illustrate the computational complexity by showing the algebraic expression with respect to the number of perception nodes (PNs).

To calculate the overall FLOPs of a model, convolution layers and fully connected layers are mainly considered, which can be calculated by the following equations:

$$\mathcal{F}(conv) = 2 \times \mathcal{C} \times \mathcal{S} \times \mathcal{O} \tag{14}$$

$$\mathcal{F}(linear) = 2 \times \mathcal{I} \times \mathcal{O} \tag{15}$$

where \mathcal{C} , \mathcal{S} , \mathcal{I} , and \mathcal{O} represent the number of channels, kernel shape, input shape, and output shape, respectively.

The computational complexity for different models is calculated and shown in Table 6 and 7. Table 6 shows the GFLOPs (one billion FLOPs) for each model under three different perception conditions: 1) no cooperation, 2) ego-centric cooperative perception with 10 perception nodes, and 3) holistic cooperative perception with 10 perception

Table 6: GFLOPs analysis under different cooperative perception conditions.

Model	GFLOPs	VINet(Ours)	EarlyFusion	LateFusion	F-Cooper	PillarGrid
Encoder	No cooperation	19.88	0.55	0.55	0.55	0.55
	Egocentric CP w/ 10 PN	198.80	5.50	5.50	5.50	5.50
	Holistic CP w/ 10 PN	198.80	5.50	5.50	5.50	5.50
Backbone	No cooperation	270.58	289.91	289.91	289.91	289.91
	Egocentric CP w/ 10 PN	270.58	289.91	2,899.10	2,899.10	2,899.10
	Holistic CP w/ 10 PN	270.58	2,899.10	2,899.10	2,899.10	2,899.10
Head	No cooperation	4.83	4.83	4.83	4.83	4.83
	Egocentric CP w/ 10 PN	4.83	4.83	48.30	4.83	4.83
	Holistic CP w/ 10 PN	4.83	48.30	48.30	48.30	48.30
Overall	No cooperation	295.29	295.29	295.29	295.29	295.29
	Egocentric CP w/ 10 PN	474.21	295.29	2,952.90	2,909.43	2,909.43
	Holistic CP w/ 10 PN	474.21	2,952.90	2,952.90	2,952.90	2,952.90

Table 7: Computational complexity under different cooperative perception conditions.

Model	Complexity	VINet(Ours)	EarlyFusion	LateFusion	F-Cooper	PillarGrid
Encoder	Egocentric Coop. w/ 10 PN	$\mathcal{O}(N)$	$\mathcal{O}(1)$	$\mathcal{O}(N)$	$\mathcal{O}(N)$	$\mathcal{O}(N)$
	Holistic Coop. w/ 10 PN	$\mathcal{O}(N)$	$\mathcal{O}(N)$	$\mathcal{O}(N)$	$\mathcal{O}(N)$	$\mathcal{O}(N)$
Backbone	Egocentric Coop. w/ 10 PN	$\mathcal{O}(1)$	$\mathcal{O}(1)$	$\mathcal{O}(K)$	$\mathcal{O}(K)$	$\mathcal{O}(K)$
	Holistic Coop. w/ 10 PN	$\mathcal{O}(1)$	$\mathcal{O}(K)$	$\mathcal{O}(K)$	$\mathcal{O}(K)$	$\mathcal{O}(K)$
Head	Egocentric Coop. w/ 10 PN	$\mathcal{O}(1)$	$\mathcal{O}(1)$	$\mathcal{O}(M)$	$\mathcal{O}(1)$	$\mathcal{O}(1)$
	Holistic Coop. w/ 10 PN	$\mathcal{O}(1)$	$\mathcal{O}(M)$	$\mathcal{O}(M)$	$\mathcal{O}(M)$	$\mathcal{O}(M)$
Overall	Egocentric Coop. w/ 10 PN	$\mathcal{O}(N)$	$\mathcal{O}(N)$	$\mathcal{O}(N + K + M)$	$\mathcal{O}(N + K)$	$\mathcal{O}(N + K)$
	Holistic Coop. w/ 10 PN	$\mathcal{O}(N)$	$\mathcal{O}(N + K + M)$	$\mathcal{O}(N + K + M)$	$\mathcal{O}(N + K + M)$	$\mathcal{O}(N + K + M)$

nodes. The results demonstrated that our method can reduce the GFLOPs by a large margin under holistic CP conditions. Even under egocentric CP conditions, in which the EarlyFusion method can be regarded as the lowest boundary of the required GFLOPs, our method performs quite close to that boundary.

In addition, Table 7 demonstrates the computational complexity with theoretically concise notations. Our method can achieve constant complexity for the backbone and head and linear complexity for the encoder. On the other hand, most of the compared methods have a linear complexity for the backbone module, i.e. $\mathcal{O}(K)$, which extremely increases the total GFLOPs of the model.

5.1.2 Communication Complexity

To theoretically analyze the communication complexity, megabytes (MB) can be used for evaluating the data size that needed to be transmitted via communication. Since metadata transmission requires much less communication bandwidth than feature data transmission, in this study, the system communication cost is mainly estimated based on feature data transmission. VINet is the first CP method that offers linear communication complexity.

Therefore, the communication complexity can be calculated as:

$$\begin{aligned}
 \mathcal{M}_{vinet}(N) &= N \times m_{vinet} \\
 \mathcal{M}_{early}(N) &= N \times (N - 1) \times m_{early} \\
 \mathcal{M}_{dense}(N) &= N \times (N - 1) \times m_{dense}
 \end{aligned} \tag{16}$$

where m_{vinet} , m_{early} , and m_{dense} represent the bandwidth cost per channel for VINet, EarlyFusion, and F-Cooper, respectively. Specifically, m_{early} is based on the statement in [61], while m_{vinet} and m_{dense} are calculated based on their feature size. Thus, the communication complexity for different methods can be summarized in Table 8. Getting

benefit from the global CP structure, VINet is the only method that can achieve linear complexity for communication under holistic CP conditions.

Table 8: Communication complexity under different cooperative perception conditions.

MB	VINet	EarlyFusion	F-Cooper	PillarGrid
Single Transmission	$\mathcal{O}(1)$	$\mathcal{O}(1)$	$\mathcal{O}(1)$	$\mathcal{O}(1)$
Egocentric Coop. w/ 10 PNs	$\mathcal{O}(N)$	$\mathcal{O}(N)$	$\mathcal{O}(N)$	$\mathcal{O}(N)$
Holistic Coop. w/ 10 PNs	$\mathcal{O}(N)$	$\mathcal{O}(N^2)$	$\mathcal{O}(N^2)$	$\mathcal{O}(N^2)$

5.2 Experimental Cost Analysis

In this paper, we also conduct real-world experiments to analyze the system-level cost. Since the capacity of GPU memory and communication bandwidth cost are crucial factors for the real-world implementation of the deep network-based method and cooperative perception, respectively, these two factors are analyzed by real-world evaluation and estimation.

5.2.1 GPU Cost Estimation

In this study, we use GPU memory consumption as a surrogate and propose a polynomial model to estimate the system-wide computational costs with limited computational power, in a mathematical manner.

We can start the analysis from the single-node perception process, which can be divided into three main components in terms of the computing process: 1) the voxelization and pillar encoder, 2) the pillar scatters and CNN backbone and 3) the detection head. We denote the computational costs of these computing processes to be \mathcal{E} , \mathcal{B} , and \mathcal{D} , respectively. Then a polynomial model for single-node perception can be designed as:

$$\mathcal{E} + \mathcal{B} + \mathcal{D} = \mathcal{C}_{single} \quad (17)$$

According to Table 11, the VINet computing process can be divided into three phases: 1) GPP + LEF on LCU, 2) TSF + CFB on CCU, and 3) 3DH on CCU. For CP system with N nodes, the computational cost can be defined as:

$$N \times \mathcal{E} + \mathcal{B} + \mathcal{D} = \mathcal{C}_{vinet} \quad (18)$$

Furthermore, for the dense-feature-based CP methods [18], the fusion happens after the CNN backbone. So their computational cost can be defined as:

$$N \times (\mathcal{E} + \mathcal{B}) + \mathcal{D} = \mathcal{C}_{dense} \quad (19)$$

Both early fusion and late fusion need \mathcal{C}_{single} for each perception node, thus their computational cost can be defined as:

$$N \times (\mathcal{E} + \mathcal{B} + \mathcal{D}) = \mathcal{C}_{early/late} \quad (20)$$

For the CARTI dataset in this paper, we have 2 to 7 perception nodes collected randomly. Here we assume an average number of PNs, i.e., $N = 4$ to process the testing results for GPU memory cost. During the inference with *batchsize* of 1, $\tilde{\mathcal{C}}_{early}$, $\tilde{\mathcal{C}}_{vinet}$ and $\tilde{\mathcal{C}}_{dense}$ are measured as 12.52, 5.60, and 10.95, respectively (in GB). Therefore, by solving the aforementioned polynomial equations, we will get:

$$\begin{aligned} \mathcal{E} &= 0.823 \\ \mathcal{B} &= 1.783 \\ \mathcal{D} &= 0.520 \end{aligned} \quad (21)$$

Thus, we can get the polynomial representation of the system-wide cost estimation for the models mentioned above:

$$\begin{aligned} \mathcal{C}_{single}(N) &= 3.13 \\ \mathcal{C}_{vinet}(N) &= 0.82 \times N + 2.30 \\ \mathcal{C}_{dense}(N) &= 2.61 \times N + 0.52 \\ \mathcal{C}_{early/late}(N) &= 3.13 \times N \end{aligned} \quad (22)$$

We use the inference test with *Batchsize*= 1 which can be regarded as the way they work in the real world. Since the CARTI dataset contains 2 to 7 PNs, we use the average system-wide cost for the CARTI dataset testing results as shown in Table 9. The estimation at 10 PNs is also listed in Table 9.

Table 9: GPU memory cost analysis under different cooperative perception conditions.

GPU Memo. [GB]	Shallow Feature(Ours)	Early Feature	Dense Feature	Late Feature
No Cooperation	3.13	3.13	3.13	3.13
Egocentric Coop. Avg.	5.60	3.13	10.85	12.52
Holistic Coop. Avg. Est.	5.60	12.52	12.52	12.52
Egocentric Coop. w/10PN Est.	10.50	3.13	26.52	31.30
Holistic Coop. w/10PN Est.	10.50	31.30	31.30	31.30

In Table 9, we use *Shallow Feature* – the lightweight feature from the Encoder – to distinguish our methods with *Dense Feature* – the normally used deep feature from the Backbone [18, 21]. Under egocentric CP conditions, the GPU memory consumption of shallow feature-based methods is 48.4% and 55.3% lower than the dense feature-based and late feature-based methods on average. If 10 PNs are involved in the egocentric CP system, our method can reduce GPU memory consumption by 60.4% and 66.5% with respect to dense feature-based and late feature-based methods, respectively. Under holistic CP conditions, our method can reduce 66.5% GPU memory consumption compared with all the other methods.

In addition, Figure 6 demonstrates the change in GPU Memory Cost with different PNs involved in the CP system. It is shown that shallow features are very efficient in terms of GPU memory consumption. Although the early feature requires the lowest GPU memory under egocentric CP conditions, its GPU cost is the same as the late feature and dense feature due to its fundamental system structure.

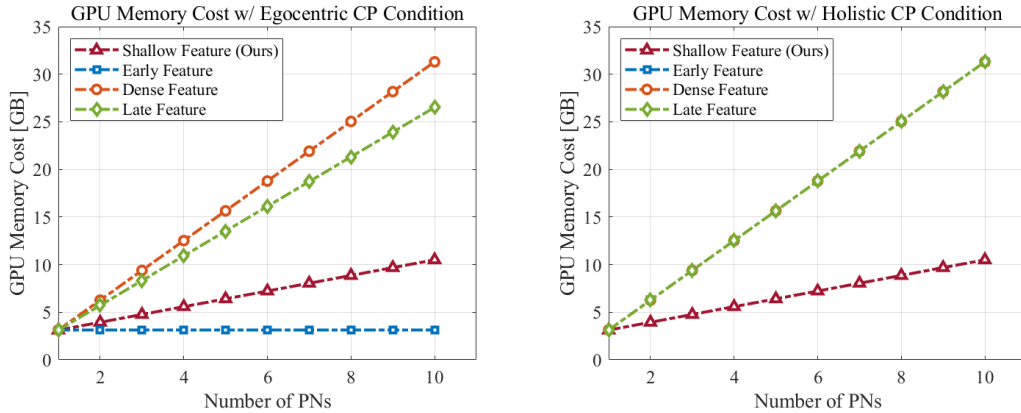


Figure 6: GPU Memory Cost under different CP Condition.

5.2.2 Bandwidth Cost Estimation

For bandwidth cost, we estimate the data size of the feature needed to be transmitted. Specifically, the size for feature per transmission can be roughly formulated using the following equation:

$$m = \frac{f \times c \times b}{1,000,000} \quad (23)$$

where f , c , and b represent the number of feature grids, the number of channels in each feature grid, and the number of bytes for each data point (4 for *float32* type used in this paper), respectively. Based on the communication complexity (see Equation 16), the bandwidth requirement analysis is shown in Table 8.

From the perspective of feature size, the shallow feature can save 35.7% data space with respect to early features, and 44.1% data space with respect to a compressed dense feature. Similar bandwidth reduction can be achieved under egocentric CP conditions. Under holistic CP conditions, our method can reduce 93.6% and 94.4% bandwidth requirements compared with early feature-based and dense feature-based methods.

²For dense-feature sharing, data compression is generally necessary to make data transmission possible. Here a $32 \times$ compression rate is assumed to F-Cooper for communication cost analysis, based on other dense-feature sharing studies, e.g., [21].

Table 10: Bandwidth requirement analysis under different cooperative perception conditions.

MB	Shallow Feature (Ours)	Early Feature	Dense Feature	Late Feature
Single Transmission	3.84	6.00	200 / 6.87 ²	0.025
Egocentric CP w/ 10 PN	34.56	54.00	61.83	0.225
Holistic CP w/ 10 PN	34.56	540.00	618.30	2.25

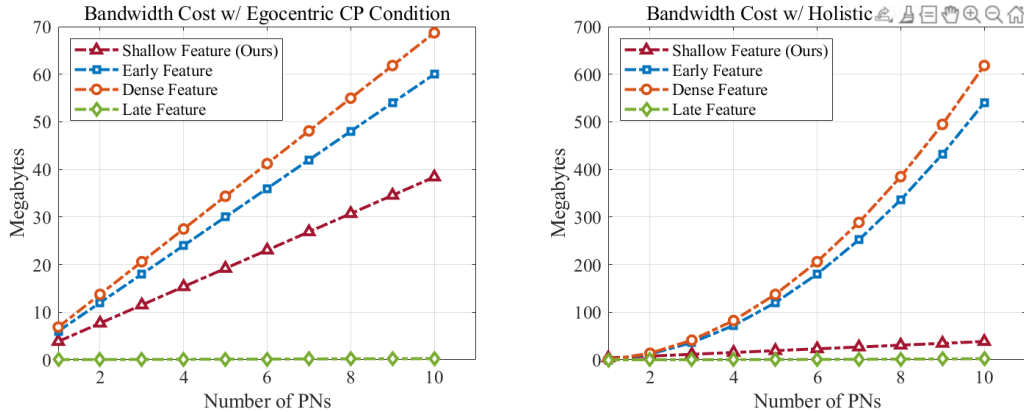


Figure 7: Bandwidth Cost under different CP Condition.

6 Conclusions

In this paper, we propose VINet, the first cooperative object detection method that is designed from the standpoint of large-scale system-level implementation. We demonstrate that for lightweight, scalable, and heterogeneous cooperative 3D object detection tasks, VINet can enhance overall mAP by 1.7% - 18.9% for car and pedestrian classes, while reducing system-wide computational costs by 84% and communication costs by 94%. Furthermore, VINet also offers a unified framework for cooperative object detection with low system-wide costs. For future work, data compression, impacts of noise levels, and latency will be further investigated to evaluate the performance of VINet under more challenging environments.

7 Acknowledgments

This research was funded by Toyota Motor North America, InfoTech Labs. The contents of this paper reflect the views of the authors only, who are responsible for the facts and the accuracy of the data presented herein. The contents do not necessarily reflect the official views of Toyota Motor North America.

References

- [1] U. D. of Transportation, Overview of motor vehicle crashes in 2019, Available: <https://crashstats.nhtsa.dot.gov/Api/Public/Publication/813060> (2020).
- [2] INRIX, Inrix: Congestion costs each american 97 hours, \$1,348 a year, Available: <https://inrix.com/press-releases/scorecard-2018-us/> (2018).
- [3] U. D. of Energy, Fotw #1204: Fuel wasted due to u.s. traffic congestion in 2020 cut in half from 2019 to 2020, Available: <https://www.energy.gov/eere/vehicles/articles/fotw-1204-sept-20-2021-fuel-wasted-due-us-traffic-congestion-2020-cut-half> (2021).
- [4] D. J. Fagnant, K. Kockelman, Preparing a nation for autonomous vehicles: opportunities, barriers and policy recommendations, *Transportation Research Part A: Policy and Practice* 77 (2015) 167–181.
- [5] S. of Automotive Engineers (SAE), Taxonomy and definitions for terms related to cooperative driving automation for on-road motor vehicles, Available: https://www.sae.org/standards/content/j3216_202107 (2021).

- [6] J. Wu, H. Xu, Y. Zhang, R. Sun, An improved vehicle-pedestrian near-crash identification method with a roadside lidar sensor, *Journal of safety research* 73 (2020) 211–224.
- [7] Z. Bai, P. Hao, W. Shanguan, B. Cai, M. J. Barth, Hybrid reinforcement learning-based eco-driving strategy for connected and automated vehicles at signalized intersections, *IEEE Transactions on Intelligent Transportation Systems* (2022) 1–14doi:10.1109/TITS.2022.3145798.
- [8] Z. Wang, Y. Bian, S. E. Shladover, G. Wu, S. E. Li, M. J. Barth, A survey on cooperative longitudinal motion control of multiple connected and automated vehicles, *IEEE Intelligent Transportation Systems Magazine* 12 (1) (2020) 4–24. doi:10.1109/MITS.2019.2953562.
- [9] L. Liu, W. Ouyang, X. Wang, P. Fieguth, J. Chen, X. Liu, M. Pietikäinen, Deep learning for generic object detection: A survey, *International journal of computer vision* 128 (2) (2020) 261–318.
- [10] E. Arnold, O. Y. Al-Jarrah, M. Dianati, S. Fallah, D. Oxtoby, A. Mouzakitis, A survey on 3d object detection methods for autonomous driving applications, *IEEE Transactions on Intelligent Transportation Systems* 20 (10) (2019) 3782–3795.
- [11] A. Manjunath, Y. Liu, B. Henriques, A. Engstle, Radar based object detection and tracking for autonomous driving, in: 2018 IEEE MTT-S International Conference on Microwaves for Intelligent Mobility (ICMIM), 2018, pp. 1–4. doi:10.1109/ICMIM.2018.8443497.
- [12] E. Yurtsever, J. Lambert, A. Carballo, K. Takeda, A survey of autonomous driving: Common practices and emerging technologies, *IEEE access* 8 (2020) 58443–58469.
- [13] Waymo, Introducing the 5th-generation waymo driver: Informed by experience, designed for scale, engineered to tackle more environments, Available: <https://blog.waymo.com/2020/03/introducing-5th-generation-waymo-driver.html> (2022).
- [14] E. Lindholm, J. Nickolls, S. Oberman, J. Montrym, Nvidia tesla: A unified graphics and computing architecture, *IEEE micro* 28 (2) (2008) 39–55.
- [15] Z. Bai, S. P. Nayak, X. Zhao, G. Wu, M. J. Barth, X. Qi, Y. Liu, K. Oguchi, Cyber mobility mirror: Deep learning-based real-time 3d object perception and reconstruction using roadside lidar, *arXiv preprint arXiv:2202.13505* (2022).
- [16] J. Zhao, H. Xu, H. Liu, J. Wu, Y. Zheng, D. Wu, Detection and tracking of pedestrians and vehicles using roadside lidar sensors, *Transportation research part C: emerging technologies* 100 (2019) 68–87.
- [17] E. Arnold, M. Dianati, R. de Temple, S. Fallah, Cooperative perception for 3d object detection in driving scenarios using infrastructure sensors, *IEEE Transactions on Intelligent Transportation Systems* (2020).
- [18] Q. Chen, X. Ma, S. Tang, J. Guo, Q. Yang, S. Fu, F-cooper: Feature based cooperative perception for autonomous vehicle edge computing system using 3d point clouds, in: *Proceedings of the 4th ACM/IEEE Symposium on Edge Computing, SEC '19*, Association for Computing Machinery, New York, NY, USA, 2019, p. 88–100. doi:10.1145/3318216.3363300. URL <https://doi.org/10.1145/3318216.3363300>
- [19] Z. Bai, G. Wu, M. J. Barth, Y. Liu, E. A. Sisbot, K. Oguchi, Pillargrid: Deep learning-based cooperative perception for 3d object detection from onboard-roadside lidar, in: 2022 IEEE 25th International Conference on Intelligent Transportation Systems (ITSC), IEEE, 2022, pp. 1743–1749.
- [20] T.-H. Wang, S. Manivasagam, M. Liang, B. Yang, W. Zeng, R. Urtasun, V2vnet: Vehicle-to-vehicle communication for joint perception and prediction, in: *European Conference on Computer Vision*, Springer, 2020, pp. 605–621.
- [21] R. Xu, H. Xiang, Z. Tu, X. Xia, M.-H. Yang, J. Ma, V2x-vit: Vehicle-to-everything cooperative perception with vision transformer, *arXiv preprint arXiv:2203.10638* (2022).
- [22] Q. Chen, S. Tang, Q. Yang, S. Fu, Cooper: Cooperative perception for connected autonomous vehicles based on 3d point clouds, in: 2019 IEEE 39th International Conference on Distributed Computing Systems (ICDCS), IEEE, 2019, pp. 514–524.
- [23] S. M. Ahmed, C. M. Chew, Density-based clustering for 3d object detection in point clouds, in: *Proceedings of the IEEE/CVF Conference on Computer Vision and Pattern Recognition*, 2020, pp. 10608–10617.
- [24] Z. Zhang, L. Zhang, X. Tong, P. T. Mathiopoulos, B. Guo, X. Huang, Z. Wang, Y. Wang, A multilevel point-cluster-based discriminative feature for als point cloud classification, *IEEE Transactions on Geoscience and Remote Sensing* 54 (6) (2016) 3309–3321.
- [25] G. Bishop, G. Welch, et al., An introduction to the kalman filter, *Proc of SIGGRAPH, Course 8* (27599-23175) (2001) 41.

- [26] Z. Zhang, J. Zheng, H. Xu, X. Wang, Vehicle detection and tracking in complex traffic circumstances with roadside lidar, *Transportation research record* 2673 (9) (2019) 62–71.
- [27] Z. Zhang, J. Zheng, H. Xu, X. Wang, X. Fan, R. Chen, Automatic background construction and object detection based on roadside lidar, *IEEE Transactions on Intelligent Transportation Systems* 21 (10) (2019) 4086–4097.
- [28] C. R. Qi, L. Yi, H. Su, L. J. Guibas, Pointnet++: Deep hierarchical feature learning on point sets in a metric space, *Advances in neural information processing systems* 30 (2017).
- [29] S. Shi, X. Wang, H. Li, Pointcnn: 3d object proposal generation and detection from point cloud, in: *Proceedings of the IEEE/CVF conference on computer vision and pattern recognition*, 2019, pp. 770–779.
- [30] S. Shi, C. Guo, L. Jiang, Z. Wang, J. Shi, X. Wang, H. Li, Pv-rcnn: Point-voxel feature set abstraction for 3d object detection, in: *Proceedings of the IEEE/CVF Conference on Computer Vision and Pattern Recognition*, 2020, pp. 10529–10538.
- [31] Y. Zhou, O. Tuzel, Voxelnet: End-to-end learning for point cloud based 3d object detection, in: *Proceedings of the IEEE conference on computer vision and pattern recognition*, 2018, pp. 4490–4499.
- [32] Y. Yan, Y. Mao, B. Li, Second: Sparsely embedded convolutional detection, *Sensors* 18 (10) (2018) 3337.
- [33] A. H. Lang, S. Vora, H. Caesar, L. Zhou, J. Yang, O. Beijbom, Pointpillars: Fast encoders for object detection from point clouds, in: *Proceedings of the IEEE/CVF Conference on Computer Vision and Pattern Recognition*, 2019, pp. 12697–12705.
- [34] M. Simony, S. Milzy, K. Amendey, H.-M. Gross, Complex-yolo: An euler-region-proposal for real-time 3d object detection on point clouds, in: *Proceedings of the European Conference on Computer Vision (ECCV) Workshops*, 2018, pp. 0–0.
- [35] B. Yang, W. Luo, R. Urtasun, Pixor: Real-time 3d object detection from point clouds, in: *Proceedings of the IEEE conference on Computer Vision and Pattern Recognition*, 2018, pp. 7652–7660.
- [36] H. Lu, X. Chen, G. Zhang, Q. Zhou, Y. Ma, Y. Zhao, Scanet: Spatial-channel attention network for 3d object detection, in: *ICASSP 2019-2019 IEEE International Conference on Acoustics, Speech and Signal Processing (ICASSP)*, IEEE, 2019, pp. 1992–1996.
- [37] Z. Liu, H. Tang, A. Amini, X. Yang, H. Mao, D. Rus, S. Han, Bevfusion: Multi-task multi-sensor fusion with unified bird’s-eye view representation, *arXiv preprint arXiv:2205.13542* (2022).
- [38] Z. Bai, G. Wu, X. Qi, Y. Liu, K. Oguchi, M. J. Barth, Infrastructure-based object detection and tracking for cooperative driving automation: A survey, in: *2022 IEEE Intelligent Vehicles Symposium (IV)*, IEEE, 2022, pp. 1366–1373.
- [39] J. Wu, H. Xu, J. Zheng, Automatic background filtering and lane identification with roadside lidar data, in: *2017 IEEE 20th International Conference on Intelligent Transportation Systems (ITSC)*, IEEE, 2017, pp. 1–6.
- [40] J. Li, J.-h. Cheng, J.-y. Shi, F. Huang, Brief introduction of back propagation (bp) neural network algorithm and its improvement, in: *Advances in computer science and information engineering*, Springer, 2012, pp. 553–558.
- [41] Y. Cui, H. Xu, J. Wu, Y. Sun, J. Zhao, Automatic vehicle tracking with roadside lidar data for the connected-vehicles system, *IEEE Intelligent Systems* 34 (3) (2019) 44–51.
- [42] J. Zhang, W. Xiao, B. Coifman, J. P. Mills, Vehicle tracking and speed estimation from roadside lidar, *IEEE Journal of Selected Topics in Applied Earth Observations and Remote Sensing* 13 (2020) 5597–5608.
- [43] S. J. Julier, J. K. Uhlmann, Unscented filtering and nonlinear estimation, *Proceedings of the IEEE* 92 (3) (2004) 401–422.
- [44] Y. Bar-Shalom, F. Daum, J. Huang, The probabilistic data association filter, *IEEE Control Systems Magazine* 29 (6) (2009) 82–100.
- [45] L. Zhang, J. Zheng, R. Sun, Y. Tao, Gc-net: Gridding and clustering for traffic object detection with roadside lidar, *IEEE Intelligent Systems* (2020).
- [46] Y. Song, H. Zhang, Y. Liu, J. Liu, H. Zhang, X. Song, Background filtering and object detection with a stationary lidar using a layer-based method, *IEEE Access* 8 (2020) 184426–184436. doi:10.1109/ACCESS.2020.3029341.
- [47] M. Gouda, B. Arantes de Achilles Mello, K. El-Basyouny, Automated object detection, mapping, and assessment of roadside clear zones using lidar data, *Transportation research record* 2675 (12) (2021) 432–448.
- [48] Z. Zhang, J. Zheng, X. Wang, X. Fan, Background filtering and vehicle detection with roadside lidar based on point association, in: *2018 37th Chinese Control Conference (CCC)*, 2018, pp. 7938–7943. doi:10.23919/ChiCC.2018.8484040.

- [49] Z. Bai, G. Wu, X. Qi, Y. Liu, K. Oguchi, M. J. Barth, Cyber mobility mirror for enabling cooperative driving automation in mixed traffic: A co-simulation platform, *IEEE Intelligent Transportation Systems Magazine* (2022).
- [50] A. Dosovitskiy, G. Ros, F. Codevilla, A. Lopez, V. Koltun, Carla: An open urban driving simulator, in: *Conference on robot learning*, PMLR, 2017, pp. 1–16.
- [51] B. Veeramani, J. W. Raymond, P. Chanda, Deepsort: deep convolutional networks for sorting haploid maize seeds, *BMC bioinformatics* 19 (9) (2018) 1–9.
- [52] Z. Gong, Z. Wang, B. Zhou, W. Liu, P. Liu, Pedestrian detection method based on roadside light detection and ranging, *SAE International Journal of Connected and Automated Vehicles* 4 (12-04-04-0031) (2021).
- [53] E. E. Marvasti, A. Raftari, A. E. Marvasti, Y. P. Fallah, R. Guo, H. Lu, Cooperative lidar object detection via feature sharing in deep networks, in: *2020 IEEE 92nd Vehicular Technology Conference (VTC2020-Fall)*, IEEE, 2020, pp. 1–7.
- [54] R. Xu, H. Xiang, X. Xia, X. Han, J. Liu, J. Ma, Opv2v: An open benchmark dataset and fusion pipeline for perception with vehicle-to-vehicle communication, *arXiv preprint arXiv:2109.07644* (2021).
- [55] Z. Bai, G. Wu, M. J. Barth, Y. Liu, E. A. Sisbot, K. Oguchi, Z. Huang, A survey and framework of cooperative perception: From heterogeneous singleton to hierarchical cooperation, *arXiv preprint arXiv:2208.10590* (2022).
- [56] Z. Zhang, S. Wang, Y. Hong, L. Zhou, Q. Hao, Distributed dynamic map fusion via federated learning for intelligent networked vehicles, in: *2021 IEEE International Conference on Robotics and Automation (ICRA)*, IEEE, 2021, pp. 953–959.
- [57] S. Ren, K. He, R. Girshick, J. Sun, Faster R-CNN: towards real-time object detection with region proposal networks, *IEEE transactions on pattern analysis and machine intelligence* 39 (6) (2016) 1137–1149.
- [58] Open-mmlab, MMDetection3D: OpenMMLab next-generation platform for general 3D object detection, <https://github.com/open-mmlab/mmdetection3d> (2020).
- [59] A. Geiger, P. Lenz, R. Urtasun, Are we ready for autonomous driving? the kitti vision benchmark suite, in: *2012 IEEE Conference on Computer Vision and Pattern Recognition*, 2012, pp. 3354–3361. doi:10.1109/CVPR.2012.6248074.
- [60] H. Caesar, V. Bankiti, A. H. Lang, S. Vora, V. E. Liong, Q. Xu, A. Krishnan, Y. Pan, G. Baldan, O. Beijbom, nuscenes: A multimodal dataset for autonomous driving, in: *Proceedings of the IEEE/CVF conference on computer vision and pattern recognition*, 2020, pp. 11621–11631.
- [61] J. Cui, H. Qiu, D. Chen, P. Stone, Y. Zhu, Coopernaut: End-to-end driving with cooperative perception for networked vehicles, in: *Proceedings of the IEEE/CVF Conference on Computer Vision and Pattern Recognition*, 2022, pp. 17252–17262.

A Model Details

In this supplementary material, we first provide more details about the model design and analysis, including the global transformation, loss function, and network configuration. Then, detailed information on the CARTI platform is introduced, followed by the mathematical analysis of system-wide cost estimation.

A.1 Global Transformation

Specifically, the GPP transformation can be defined as:

$$R_X = \begin{bmatrix} 1 & 0 & 0 \\ 0 & \cos(-R) & -\sin(-R) \\ 0 & \sin(-R) & \cos(-R) \end{bmatrix} \quad (24)$$

$$R_Y = \begin{bmatrix} \cos(-P) & 0 & \sin(-P) \\ 0 & 1 & 0 \\ -\sin(-P) & 0 & \cos(-P) \end{bmatrix} \quad (25)$$

$$R_Z = \begin{bmatrix} \cos(-\Theta) & -\sin(-\Theta) & 0 \\ \sin(-\Theta) & \cos(-\Theta) & 0 \\ 0 & 0 & 1 \end{bmatrix} \quad (26)$$

$$T = [X \ Y \ Z \ 0]^T \quad (27)$$

$$P^{S \rightarrow G} = \begin{bmatrix} R_X & 0 \\ 0 & 1 \end{bmatrix} \cdot \begin{bmatrix} R_Y & 0 \\ 0 & 1 \end{bmatrix} \cdot \begin{bmatrix} R_Z & 0 \\ 0 & 1 \end{bmatrix} \cdot P^S + T \quad (28)$$

where R_X , R_Y , R_Z , and T represent the rotation matrix along x -axis, y -axis, z -axis, and the translation matrix, respectively. P^S and $P^{S \rightarrow G}$ represent the PCD with respect to the sensor's coordinate and global coordinate, respectively.

A.2 Loss Function

Regarding a traditional anchor-based detection head, a 7-dimensional vector $(x, y, z, w, l, h, \theta)$ is defined for each box, where w, l, h , and θ represent the width, length, height, and yaw angle, respectively. The loss function is defined as:

$$\Delta x = \frac{x^{gt} - x^a}{d^a}, \Delta y = \frac{y^{gt} - y^a}{d^a}, \Delta z = \frac{z^{gt} - z^a}{h^a}, \quad (29)$$

$$\Delta w = \log \frac{w^{gt}}{w^a}, \Delta l = \log \frac{l^{gt}}{l^a}, \Delta h = \log \frac{h^{gt}}{h^a}, \quad (30)$$

$$\Delta \theta = \sin(\theta^{gt} - \theta^a) \quad (31)$$

where the superscript gt and a represent the ground truth and anchor, respectively; and d^a is defined by:

$$d^a = \sqrt{(w^a)^2 + (l^a)^2}. \quad (32)$$

The total localization loss is:

$$L_{loc} = \sum_{b \in (x, y, z, w, l, h, \theta)} \text{SmoothL1}(\Delta b) \quad (33)$$

The object classification loss is defined as:

$$L_{cls} = -\alpha_a (1 - p^a)^\gamma \log p^a, \quad (34)$$

where p^a is the class probability of an anchor; and α and γ are set to be 0.25 and 2, respectively. Hence, the total loss is:

$$L = \frac{1}{N_{pos}} (\beta_{loc} L_{loc} + \beta_{cls} L_{cls} + \beta_{dir} L_{dir}), \quad (35)$$

where N_{pos} is the number of positive anchors; and β_{loc} , β_{cls} and β_{dir} are set as 2, 1, and 0.2, respectively.

A.3 Architectural Specification

According to the mathematical definitions, the whole VINet model can be formulated as:

$$\begin{aligned}
 f_i &= GPP(x_i), x_i \in \mathcal{R}^{N_{all} \times 4}, & \text{for } PN_i, i = 1, \dots, N \\
 z_i &= LFE(f_i), f_i \in P_{\Omega}^{S \rightarrow G}, & \text{for } PN_i, i = 1, \dots, N \\
 z_f &= TSF(z_i), z_i \in \mathcal{R}^{P \times 64}, & \text{for Central Node} \\
 z_h &= CFB(z_f), z_f \in \mathcal{R}^{C \times W \times H}, & \text{for Central Node} \\
 y &= 3DH(z_h), & \text{for Central Node}
 \end{aligned} \tag{36}$$

where x_i represents the raw PCD for each PN. Table 11 demonstrates the detailed specification of the network structure of VINet.

Table 11: Detailed Architectural Specifications for VINet

Device	Component	Output Size	VINet Structure	
LCU	GPP	$N \times [P \times 64]$	[Voxel Encoder 0.23, 0.23, 4]	
	LEF		[Veh. MLP, 9, 64]	[Inf. MLP, 9, 64]
	TSF	$N \times P \times 64$	[Veh. Pillar Scatter (512, 1024)]	[Inf. Pillar Scatter (512, 1024)]
		$2 \times [64 \times 512 \times 1024]$	[Veh. Maxout]	[Inf. Maxout]
		$128 \times 512 \times 1024$	[Concat2, 128]	
		$64 \times 256 \times 512$	[Conv3×3, 128, 64, stride 2, BN, ReLU] × 1	
CCU	CFB	$384 \times 256 \times 512$	[Conv3×3, 64, 64, stride 1, BN, ReLU] × 3 [Conv3×3, 64, 128, stride 2, BN, ReLU] × 1 [Conv3×3, 128, 128, stride 1, BN, ReLU] × 5 [Conv3×3, 128, 256, stride 2, BN, ReLU] × 1 [Conv3×3, 256, 256, stride 1, BN, ReLU] × 5 [DeConv3×3, 64, 128, stride 1, BN, ReLU] × 1 [DeConv3×3, 128, 128, stride 2, BN, ReLU] × 1 [DeConv3×3, 256, 128, stride 4, BN, ReLU] × 1 [Concat3, 384]	
			3DH	$256 \times 512 \times 48$

B CARTI Platform

The dataset generated from the platform is named “*CARTI*” (i.e., **CAR**la-**ki**TtI). The CARTI dataset applied in this paper consists of data collected from a varying number of sensors. Specifically, two infrastructure-based LiDAR sensors and 0 to 5 vehicle-based LiDAR sensors are deployed in total. Based on our previous experience with the real-world infrastructure-based LiDAR system [15], the roadside sensor is equipped on a traffic signal pole of the intersection with a height of 4.74m. On the other hand, the onboard LiDAR sensors are mounted on top of the CAVs with a height of 1.74m based on KITTI’s settings. Figure 10 illustrates the transformation between coordinate systems in CARLA and KITTI.



Figure 8: Top-down view for the targeting area of cooperative perception.

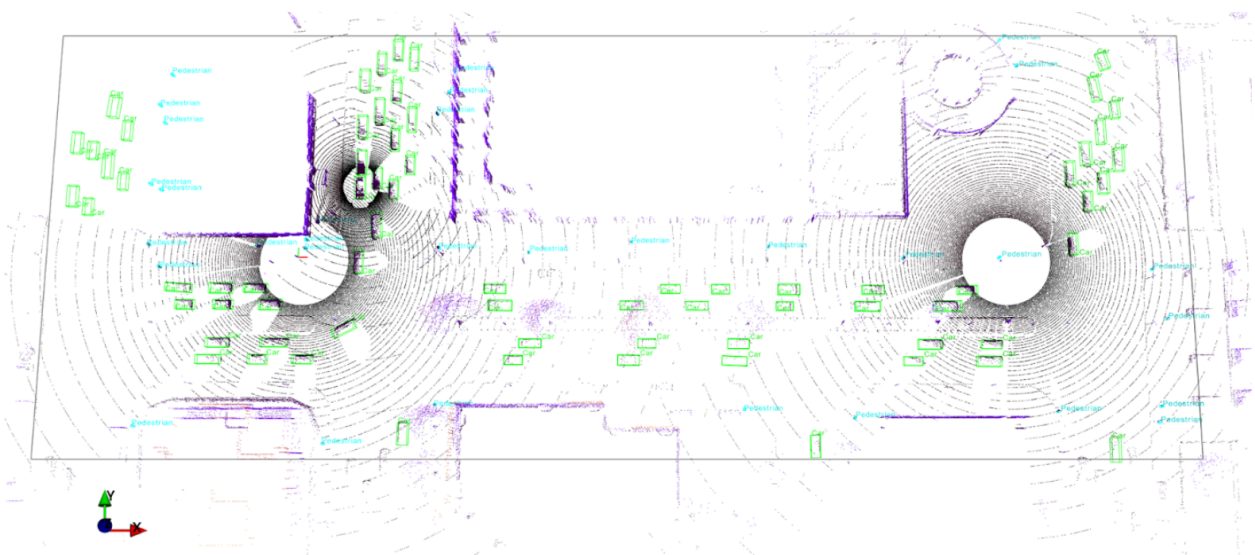


Figure 9: 3D point clouds and ground truth labels in one data frame

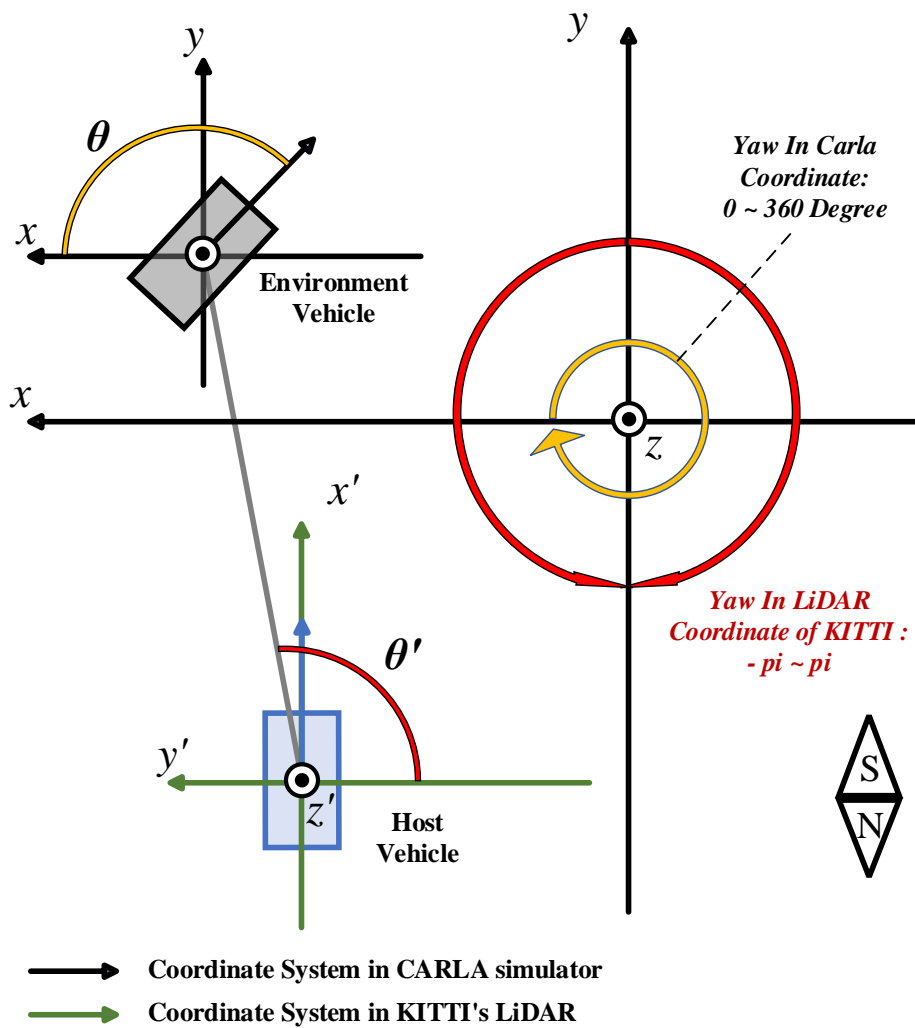


Figure 10: Visualization of data transformation from the CARLA environment to KITTI's format.